

PAPER • OPEN ACCESS

Polynomial chaos expansion of SAR and temperature increase variability in 3 T MRI due to stochastic input data

To cite this article: Oriano Bottauscio *et al* 2024 *Phys. Med. Biol.* **69** 125005

View the [article online](#) for updates and enhancements.

You may also like

- [Ultra-high field MRI: parallel-transmit arrays and RF pulse design](#)
Sydney N Williams, Paul McElhinney and Shajan Gunamony
- [Robust, planning-based targeted locoregional tumour heating in small animals](#)
Jort A Groen, Johannes Crezee, Hanneke W M van Laarhoven *et al.*
- [The relationship between specific absorption rate and temperature elevation in anatomically based human body models for plane wave exposure from 30 MHz to 6 GHz](#)
Akimasa Hirata, Ilkka Laakso, Takuya Oizumi *et al.*

Joining forces:
One complete
QA solution for
Dosimetry with
myQA[®], QUASAR[™]
and Radcal[®]!

The diagram is a circular graphic with a dark background and a pattern of small, colorful dots. It features four colored segments arranged in a circle: a dark blue segment at the top left labeled 'Machine QA', a green segment at the top right labeled 'Patient Specific QA', a light blue segment at the bottom right labeled 'Medical Imaging QA', and a pink segment at the bottom left labeled 'Risk Management'. In the center of this circle is a stylized human figure composed of green lines, representing a patient or a person undergoing medical imaging.



PAPER

OPEN ACCESS

RECEIVED
1 March 2024REVISED
20 May 2024ACCEPTED FOR PUBLICATION
24 May 2024PUBLISHED
7 June 2024

Original content from
this work may be used
under the terms of the
[Creative Commons
Attribution 4.0 licence](#).

Any further distribution
of this work must
maintain attribution to
the author(s) and the title
of the work, journal
citation and DOI.



Polynomial chaos expansion of SAR and temperature increase variability in 3 T MRI due to stochastic input data

Oriano Bottauscio* , Umberto Zanovello , Alessandro Arduino and Luca Zilberti

Istituto Nazionale di Ricerca Metrologica (INRIM), Torino, Italy

* Author to whom any correspondence should be addressed.

E-mail: o.bottauscio@inrim.it**Keywords:** computational electromagnetism, electromagnetic dosimetry, magnetic resonance imaging, PCE, safety, specific absorption rateSupplementary material for this article is available [online](#)

Abstract

Objective. Numerical simulations are largely adopted to estimate dosimetric quantities, e.g. specific absorption rate (SAR) and temperature increase, in tissues to assess the patient exposure to the radiofrequency (RF) field generated during magnetic resonance imaging (MRI). Simulations rely on reference anatomical human models and tabulated data of electromagnetic and thermal properties of biological tissues. However, concerns may arise about the applicability of the computed results to any phenotype, introducing a significant degree of freedom in the simulation input data. In addition, simulation input data can be affected by uncertainty in relative positioning of the anatomical model with respect to the RF coil. The objective of this work is to estimate the variability of SAR and temperature increase at 3 T head MRI due to different sources of variability in input data, with the final aim to associate a global uncertainty to the dosimetric outcomes.

Approach. A stochastic approach based on arbitrary Polynomial Chaos Expansion is used to evaluate the effects of several input variability's (anatomy, tissue properties, body position) on dosimetric outputs, referring to head imaging with a 3 T MRI scanner. **Main results.** It is found that head anatomy is the prevailing source of variability for the considered dosimetric quantities, rather than the variability due to tissue properties and head positioning. From knowledge of the variability of the dosimetric quantities, an uncertainty can be attributed to the results obtained using a generic anatomical head model when SAR and temperature increase values are compared with safety exposure limits. **Significance.** This work associates a global uncertainty to SAR and temperature increase predictions, to be considered when comparing the numerically evaluated dosimetric quantities with reference exposure limits. The adopted methodology can be extended to other exposure scenarios for MRI safety purposes.

1. Introduction

Magnetic resonance imaging (MRI) is a largely used clinical imaging modality. Despite being an overall safe technique, standards exist to limit the power deposition in human tissues caused by the interactions between the radiofrequency (RF) magnetic fields used for imaging and the human body. The metric adopted to evaluate the risk of temperature increase in body tissues is the specific absorption rate (SAR) (IEC 60601-2-33:2022 2022). Commercially available MRI scanners allow automatic whole-body and partial-body SAR estimations when a specific imaging protocol is selected and warn the operator if regulatory limits are likely to be exceeded. These parameters are introduced to limit the temperature increase of tissues, which is caused by the spatial distribution of the local SAR within the body, a quantity that is not directly measurable.

Calculation of local SAR distributions in human subjects and consequent temperature increase (ΔT) of tissues, is a widely adopted strategy to complement and support safety analyses. Simulations require properly designed software and sophisticated digital models of the human body. For the latter, reference anatomical

human models are commonly adopted but concerns may arise about the applicability of the computed results to any phenotype. To manage this issue, one possible strategy is to collect data by simulating a wide range of human model categories (e.g. males/females, neonates/child/adults/elderly) accounting for anatomy variability. In this way, SAR and ΔT variability's can be estimated as a function of the influence factors selected to identify the categories, to provide adequate safety margin for the patient undergoing examination. The results that appear to be more relevant to the specific patient can be extracted from the database, also using Artificial Intelligence based techniques. A non-exhaustive list of studies following this approach is collected in the references. Referring to clinical 1.5 T / 3 T scanners, studies were conducted on SAR deposition in children/neonates compared to adults. For instance, Murbach *et al* (2011) investigated if children and foetuses are at higher risks than adults when the current RF regulations are applied to a 1.5 T whole-body coil. Malik *et al* (2015) found that SAR induced by whole-body RF coils at 1.5 T and 3 T in neonatal subjects is less than that experienced in an adult in all scenarios. In Liu *et al* (2005), a numerical model of a female body was developed to study the effects of different body types on B_1^+ and SAR distribution at 64 MHz and 128 MHz. The results showed the dependence of dosimetric quantities on body type and therefore the need for a variety of numerical models, representative of a broad population. The SAR deposition due to whole-body 3 T multi-transmit body coil was investigated in Neufeld *et al* (2011), showing a strong dependence on anatomy and leading the authors to suggest that patient-specific analysis is necessary to avoid injuries by such systems.

Due to the peculiar effects at high field MRI, several studies have been developed on the effect of anatomy on SAR deposition in 7 T scanners. For example, in de Greef *et al* (2013), RF fields generated by an eight-channel head transmit array for a 7 T scanner were simulated with six detailed head models, showing that a safety factor of 1.4 applied to prediction with a generic head model was found sufficient as a practical alternative to patient-specific models. A safety factor (from 1.8 to 2) was found necessary by Meliàdò *et al* (2019) to cover the intersubject variability when a safety assessment for 7 T prostate imaging with an eight-channel transmit array is performed using only one model.

As an alternative approach to the use of digital datasets, subject-specific digital models can be constructed to perform detailed SAR simulations. To this end, in Homann *et al* (2011), a novel approach is proposed for generating personalized body models from whole-body water-fat-separated magnetic resonance (MR) data and applied to volunteers for SAR predictions at 3 T. Subject-specific 3 T head SAR maps, derived only from the information given by the B_1^+ field, were determined in Martínez *et al* (2023) through electrical properties tomography (EPT) techniques. Then, suitable correction factors, calibrated to compensate for the missing information about the induced electric field, were introduced. The feasibility of estimating SAR in real time is shown in Gokyar *et al* (2021), where SAR maps are predicted from MR images simulated at 3 T and 7 T in 10 realistic human body models via a convolutional neural network.

Subject-specific digital models are also proposed for 7 T MRI. Jin *et al* (2012) propose the use of image registration techniques, in conjunction with high resolution image and tissue libraries, to create patient-specific voxel models to be used for subject-specific simulations. In Brink *et al* (2022), it is shown how a subject-specific body model can be automatically generated from a single T1-weighted dataset by means of deep learning techniques, providing the required inputs for accurate and personalized local SAR predictions.

Despite the promising attempts to develop a subject-specific SAR analysis, definitions of safety criteria based on simulations which use generic anatomical datasets are still largely adopted and useful, leading to the need for determining their reliability in terms of accuracy and applicability to a wide range of exposure scenarios.

A large literature exists aiming at evaluating the accuracy of computations and to establish the parameters which most affect the results. Some studies focus the attention on model refinement effects (Wolf *et al* 2013, Shao *et al* 2015a, Fiedler *et al* 2018); other works address the problem of increasing the tissue segmentation details (Carluccio *et al* 2021, de Buck *et al* 2021), or the effect of model complexity (e.g. thermoregulation for heating prediction) (Murbach *et al* 2016) or the effect of RF coil type (Lucano *et al* 2018). Further factors could also affect the SAR prediction, such as human body positioning within the RF coil, which demonstrated to play an important role (Murbach *et al* 2014).

It must also be remarked that SAR and ΔT simulations rely on literature data of tissue physical properties (Gabriel *et al* 1996, Hasgall *et al* 2018). These are often determined using *ex vivo* tissue samples not completely representative of *in vivo* conditions and obtained using measurement techniques characterized by a considerable measurement uncertainty (see for example (McCann *et al* 2019)).

All the above factors entail an intrinsic uncertainty in SAR and ΔT computations that needs to be quantified to draw reliable conclusions from simulations performed on non-specific digital human models. Statistical simulation approaches are a useful tool to address this problem.

The stochastic dosimetry concept was first introduced to address the impact of random input variables in different applicative fields. Most of them are focused on the variability of electrical tissue properties and are

applied to the planning of transcranial magnetic stimulation (see Gomez *et al* 2015, Šušnjara *et al* 2020, Colella *et al* 2021) or to the evaluation of human exposure to power-frequency electric and magnetic fields (Fiocchi *et al* 2018, Lagouanelle *et al* 2024). Other examples of stochastic dosimetry are related to the analysis of random variability of the field source, for example in the exposure to 5 G technologies (Bonato *et al* 2021) or power-frequency fields (Chiaromello *et al* 2019).

In the MRI safety context, local SAR stochastic dosimetry concepts are adopted to study the variability related to tissue property, anatomy and geometry variations. Shao *et al.* propose in Shao *et al* (2015b) a statistical simulation approach to address the local SAR variability related to tissue property and geometry variations. Instead of using the Monte–Carlo (MC) method with many sample points, the unscented transform was applied with a small set of deterministic sample points.

A probabilistic analysis to study the safety factor employed to account for SAR intersubject variability versus risk relationship in head imaging at 7 T is presented in Le Garrec *et al* (2017). Based on the SAR matrices for each configuration, a multivariate second-order polynomial of the SAR versus the different parameters (model scaling and two translations) was reconstructed for different types of radiofrequency pulses. A MC calculation was then performed to compute the probability of occurrence of a given SAR value.

The applicability of an efficient whole-body individual modelling method for the assessment of 1.5 T MRI RF exposure was investigated in Liu *et al* (2019). Stochastic dosimetry using a surrogate model was adopted to evaluate SAR variability due to body misalignment and tilt in the coil.

Finally, the effect of variations in anatomical details of the human body model, dielectric tissue properties and implant geometry on predicted SAR values during MRI in a patient with a DBS implant can be found in Nguyen *et al* (2020).

In this work, we applied the polynomial chaos expansion (PCE) technique to study how the random variability of physical tissue properties and body positioning in the RF coil affects the SAR prediction during MRI of the head at 3 T and the consequent spatial distribution of ΔT . PCE is a suitable technique to be used whenever a direct MC approach results in an excessively time-consuming computation, like in most cases that require the solution of a partial differential equation (PDE). Starting from a given statistical distribution of input variables, PCE allows to determine the statistical distribution of the output variables with a limited number of numerical simulations, used in the training phase to identify the coefficients of the polynomial expansion. Details of the proposed approach are presented in section 2.

Specifically, attention is focused on the prediction of the head SAR and of the maximum local SAR (averaged over 10 g of tissue) and maximum ΔT after 900 s of exposure, both computed on the entire head tissues. The analysis is repeated for 10 different anatomical head models (five males and five females) to compare the effect of the anatomical variability with the effects of the other considered variables. Results obtained by this analysis are reported in section 3. Finally, in the discussion section an attempt to associate a global uncertainty to the dosimetric outcomes is given, accounting for the variability of the considered input data.

2. Method

2.1. PCE

PCE is a technique, initially introduced by Wiener (1938), to construct a surrogate model in the form of a high-dimensional polynomial in uncertain model parameters. It was first applied in physics and engineering by Ghanem and Spanos (1991) and generalized by Xiu and Karniadakis (2002). It represents a widely adopted technique, alternative to traditional approaches for stochastic simulation as brute-force MC simulations (e.g. Maltz and Hitzl 1979) and related approaches (e.g. latin hypercube sampling (Helton and Davis 2003)), which would require quite large computational power for complex models.

Potentialities and limitations of PCE technique are discussed in Augustin *et al* (2008). Papers (Sudret *et al* 2008, Oladyshkin *et al* 2012) demonstrate how classical PCE and its generalisation for arbitrary probability distributions (arbitrary polynomial chaos, aPC) can deliver the information required for global sensitivity analysis at low computational costs.

A non-intrusive approach was here adopted, which does not require manipulating the PDEs governing the electromagnetic and the thermal physics. Multi-dimensional aPC was implemented following the scheme proposed by Oladyshkin and Nowak (2012). Let $Y = f(\xi_1, \xi_2, \dots, \xi_N)$ denote a stochastic model with N input random variables ξ_j ($j = 1, \dots, N$), each one having its own probability distribution. The model output Y can be represented by a multivariate polynomial expansion as follows,

$$Y(\xi_1, \xi_2, \dots, \xi_N) \approx \sum_{i=1}^M \alpha_i \Phi_i(\xi_1, \xi_2, \dots, \xi_N), \quad (1)$$

where the coefficients α_i quantify the dependence of the model output Y on the input parameters $\xi_1, \xi_2, \dots, \xi_N$ along the direction Φ_i . The number of terms in the expansion (M) depends on the total number of input parameters and on the order d of the expansion, being $M = \frac{(N+d)!}{N!d!}$.

Functions Φ_i form an orthogonal basis of the space of polynomial functions of degree at most d , which are constructed as a simple product of polynomials $P^{\beta_j^i}(\xi_j)$ of degree β_j^i ,

$$\Phi_i(\xi_1, \xi_2, \dots, \xi_N) = \prod_{j=1}^N P^{\beta_j^i}(\xi_j) \quad (2)$$

$$\sum_{j=1}^N \beta_j^i \leq d, \quad i = 1, \dots, M,$$

where β_j^i is a non-negative integer index.

In the original PCE formulation, limited to random variables with Gaussian distribution, P are Hermite polynomials. The aPC, which generalizes chaos expansion techniques towards arbitrary distributions, does not require the complete knowledge of a probability density function, avoiding assigning parametric probability distributions (Oladyshkin and Nowak 2012). The adopted aPC implementation requires statistically independent input variables.

The coefficients α_i were determined by interpolating the selected output obtained from M simulations providing the spatial distribution of SAR and ΔT in the voxels of the human head model, following the procedure described in Oladyshkin and Nowak (2012).

2.2. Solver implementation

The aPC Matlab Toolbox (Oladyshkin 2024) was used in this work. This algorithm was coupled with a frequency domain Finite Element electromagnetic solver, to compute SAR distribution, and a time domain Finite Difference thermal solver, to compute the temperature increase. Both solvers were implemented in Matlab R2022b using GPU computations where parallelization is possible. The electromagnetic solver is based on the formulation proposed in Bottauscio *et al* (2015) and validated through experiments in Bottauscio *et al* (2015). The solver uses a uniform Cartesian mesh with first order elements (voxels) for the anatomical human models and a second order hexahedral mesh for the RF coil. The thermal solver is based on the approach described in Arduino (2017).

Considering the computational burden required to solve the problem analysed in this article (see section 2.4), a direct comparison of the PCE results with a brute-force MC method is not feasible, because it would require a computational time up to hundreds of days (e.g. considering an Intel Xeon Gold 6238R CPU @ 2.2 GHz, with 512 GB RAM and NVIDIA A100 GPU card). Despite the PCE technique was largely tested against MC simulations in the literature (e.g. Kimaev and Ricardez-Sandoval 2020, Xikai *et al* 2019), a comparison with a simplified electromagnetic problem was performed in this work, considering an electromagnetic problem for which an analytical solution is available (see the [appendix: 2D analytical model](#)). Despite its simplicity, the analytical model problem keeps some similarities with the problem under study, allowing the comparison of the surrogate model with a direct MC approach.

2.3. Anatomical models

Ten digital head anatomical models (five males and five females) belonging to the XCAT library (2023) were selected for the analysis to achieve a significant anatomical variability. The main characteristics of the considered models are reported in table 1.

The following anatomical districts of the head models were identified and associated to four tissue properties:

- (a) White matter (WM), Commissura anterior, Medulla oblongata, Midbrain, Pons (for all these tissues, properties are assumed to be those of WM);
- (b) Grey matter (GM), Hippocampus, Thalamus (for all these tissues, properties are assumed to be those of GM);
- (c) Cerebrospinal fluid (CSF);
- (d) Cerebellum (CB).

2.4. Problem under study

For each simulation, the head of the considered XCAT model was centred in the RF coil with the eyes in the isocenter (figure 1). The RF coil is a birdcage body coil supplied at 128 MHz (3 T) in circular polarisation mode. The coil was supplied in current-driven mode, namely a proper current phasor (amplitude and phase)

Table 1. Main characteristics of the considered XCAT digital head models sorted by increasing head mass. For the definition of the head, please refer to the next section 2.4.

XCAT model number	Age (years)	Sex	Whole body			Head mass (kg)
			Mass (kg)	Height (cm)	BMI (kg m^{-2})	
#86	36	F	52.0	169.0	18.21	4.16
#71	27	F	55.6	172.7	18.64	4.25
#151	66	F	66.4	162.0	25.30	4.42
#76	31	F	69.6	156.0	28.60	4.55
#150	18	M	62.0	176.0	20.02	4.99
#80	33	M	69.4	176.2	22.35	5.11
#147	57	F	105.8	165.1	38.81	5.18
#196	78	M	69.2	173.0	23.10	5.35
#93	44	M	92.6	75.6	28.27	5.88
#184	50	M	120	177.8	37.96	6.20

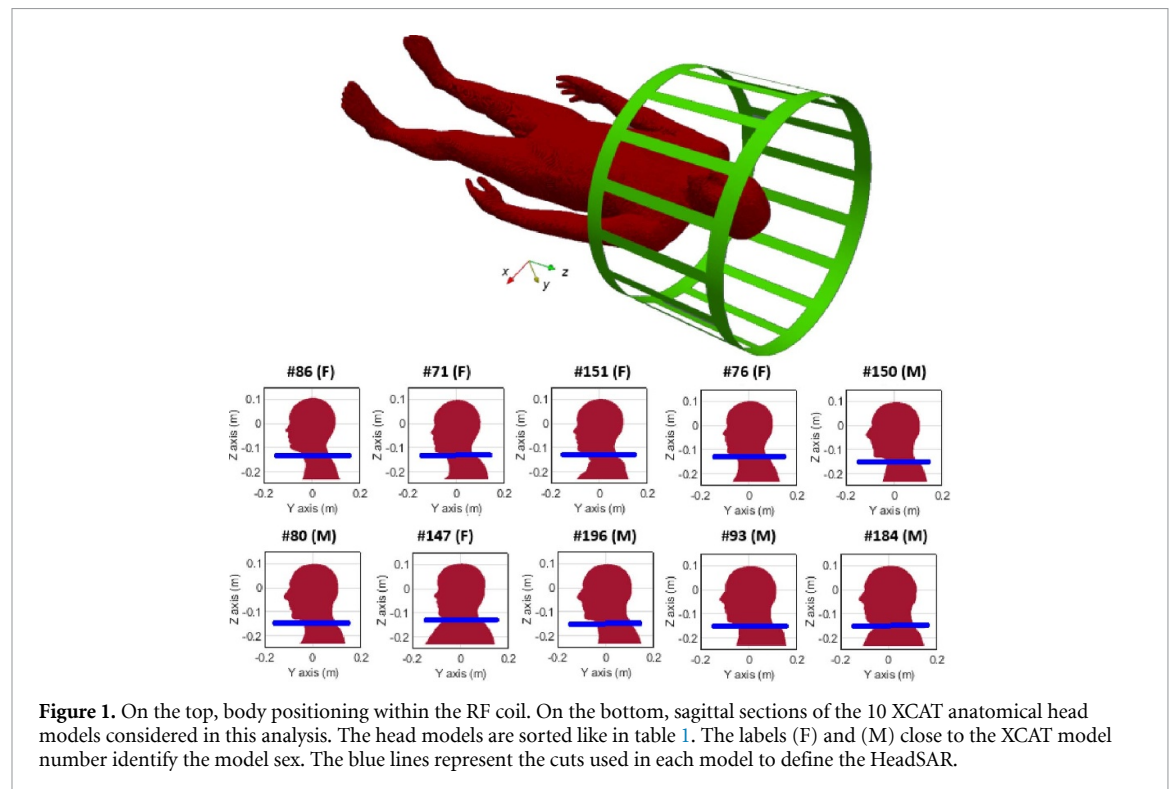


Figure 1. On the top, body positioning within the RF coil. On the bottom, sagittal sections of the 10 XCAT anatomical head models considered in this analysis. The head models are sorted like in table 1. The labels (F) and (M) close to the XCAT model number identify the model sex. The blue lines represent the cuts used in each model to define the HeadSAR.

was imposed to each leg and portion of the end-ring to obtain a uniform B_1^+ field in the imaging slice, when the head was not present.

To limit the computational burden, simulations were performed truncating the body at the level of the shoulders (outside the RF coil). This simplification has a limited impact on the spatial SAR distribution within the head region (Wolf *et al* 2013).

After each electromagnetic simulation, performed under continuous wave mode on the entire head, the spatial average value of B_1^+ magnitude was computed in a slice of thickness 40 mm around the isocenter. The choice of the slice thickness is arbitrary, but realistic for MRI imaging. Since in this work we are not interested in a direct comparison of dosimetric outcomes with safety limits, but rather in an analysis of their variability, electromagnetic field results were scaled to obtain an average value equal to $1 \mu\text{T}$.

A 900 s transient thermal simulation was performed in cascade. The spatial distribution of ΔT was computed, and the maximum temperature increase at the end of the exposure time was recorded.

Three output quantities were selected for the aPC analysis: the maximum value of local SAR averaged over 10 g (maxSAR10g), the partial body SAR in the head (HeadSAR), and the maximum value of ΔT after 900 s (max ΔT).

The local SAR averaged over 10 g, defined as the total power absorbed in a 10 g cubic volume divided by 10 g, was adopted, following the prescription of IEC 60601-2-33:2022 (2022). It was computed following the algorithm described in the ICNIRP Guidelines (2020), where a cubic averaging mass of 10 g, including all

Table 2. Coefficients of the dependence of physical properties on water percentage.

Physical property	$p_{i,1}$	$p_{i,2}$	$p_{i,3}$
σ ($i = 1$)	0.286	1.5310^{-5}	0.1185
ε_r ($i = 2$)	-0.0287	5.91	-220
λ ($i = 3$)	3.5810^{-3}	0.233	—
C ($i = 4$)	21.98	1923	—
δ ($i = 5$)	-2.030	1217	—

tissues, is used. In proximity of the interface tissue-air, the cube is extended only towards tissues, until the 10 g mass is obtained.

Regarding HeadSAR, since its value depends on the definition of ‘head’, as demonstrated in Goren *et al* (2024), in this work computation was done in accordance with the reference head definition taken by the masks described in annex P of ISO/TS 10974 (2018). This mask region includes the cranial and cervical vertebrae superior to C7.

For each considered output quantity, the coefficients α_i of the polynomial expansion of aPC were computed, allowing the estimation of the corresponding statistical distribution, along with its mean value and standard deviation. The order d of the expansion was set to 3. The stability of the surrogate models provided by aPC at the increase of the order of the expansion was assessed (see section 3.2).

The head phantoms were discretized in 2 mm voxels leading to a total number of voxels ranging from 479 761 (model #86) to 695 593 (model #184). For each SAR simulation, the computational time was variable from ~ 40 min to ~ 70 min (depending on the problem size) on an Intel Xeon Gold 6238R processor with 512 GB RAM and NVIDIA A100-PCIE-40 GB GPU card. The computational time for the thermal simulation was ~ 5 min on the same hardware.

2.5. Tissue physical properties

The effect of the variability of the physical properties (mass density, electrical conductivity and permittivity, thermal conductivity, specific heat capacity) of brain tissues (WM, GM, CSF and CB) was first studied.

Having selected only adult models, age-related biological changes (see for example (Gräfe *et al* 2021) for T1 variability from children to adults and related correlation with electrical properties (Michel *et al* 2016) are not considered here. On the contrary, the results rely only on statistical tissue properties variability among adult subjects.

For a given tissue, the considered physical properties are presumably correlated to each other depending on the tissue water content. This would affect the requirement of the aPC to work with uncorrelated input parameters. To solve this issue, tissue water content values of the four brain tissues, assumed independent one from each other, are used as input random variables.

Electrical conductivity and permittivity were modelled as a monotonic function of tissue water content percentage (W), under the principle of Maxwell’s mixture theory, as proposed in Michel *et al* (2016). For brain tissues at 128 MHz, electrical conductivity σ is provided by the following exponential function,

$$\sigma = p_{1,1} + p_{1,2} e^{p_{1,3}W} \quad (3)$$

while the relative permittivity ε_r is described by the following second-order polynomial,

$$\varepsilon_r = p_{2,1}W^2 + p_{2,2}W + p_{2,3}. \quad (4)$$

For mass density δ , thermal conductivity λ and specific heat capacity c , a linear relationship with water content is adopted, as proposed in Ahuja *et al* (1978), Vaupel and Piazena (2022). Thus,

$$\lambda = p_{3,1}W + p_{3,2} \quad (5a)$$

$$c = p_{4,1}W + p_{4,2} \quad (5b)$$

$$\delta = p_{5,1}W + p_{5,2}. \quad (5c)$$

The values of the coefficients $p_{i,j}$ are reported in table 2.

The thermal problem, being described by the bio-heat equation (Pennes 1948), depends also on the perfusion rate of the tissues. This parameter, however, was left unchanged in the aPC analysis, assuming that the perfusion rate is mainly associated with the physiopathological status of the patient, affecting its

Table 3. Reference data of the four tissues considered in the analysis.

Tissue	W_{ref} (%)	σ (S m ⁻¹)	ε_r	λ (W m ⁻¹ K ⁻¹)	c (J kg ⁻¹ K ⁻¹)	δ (kg m ⁻³)
White matter (WM)	69.57	0.344	52.3	0.482	3453	1076
Grey matter (GM)	83.41	0.587	73.3	0.531	3757	1048
Cerebrospinal fluid (CSF)	98.8	2.149	83.8	0.587	4095	1017
Cerebellum (CB)	88.43	0.831	78.2	0.549	3867	1038

thermoregulatory system, instead of the tissue water content. The effect of its variability was analysed as a standalone case.

The reference water content values and the associated physical property values, corresponding to the four identified brain tissues, are reported in table 3. WM, GM and CSF water content values are obtained from (Michel *et al* 2016). CB water content value was selected as the one that better fits the values of the physical properties provided in the IT'IS Foundation database (Hasgall *et al* 2018).

In the aPC implementation, the water content W in each tissue is assumed having a uniform distribution centred on the reference value W_{ref} with variation of $\pm W_{\text{dev}}$ (ranging from 1 % to 8 % in the following analysis), that is

$$W \sim U(W_{\text{ref}} - W_{\text{dev}}, W_{\text{ref}} + W_{\text{dev}}).$$

Being the number of input variables N equal to 4, the total number M of electromagnetic and thermal simulations required, for each XCAT model, to determine the coefficients α_i of the polynomial expansion in aPC was equal to 35.

For all other non-brain tissues in the head model, fixed values of physical properties were assigned from IT'IS Foundation database (Hasgall *et al* 2018).

2.6. Head positioning

In this second analysis, the stochastic input variables ξ_j are the six parameters describing the possible roto-translations of the reference head models with respect to the RF source. This stochastic input models the uncertain positioning of the patient within the MRI scanner, where small deviations from a reference position are admitted.

First, the axis of rotation Ψ_R was extracted from a uniform distribution on the hemisphere. This was obtained by extracting two non-dimensional numbers r and s uniformly distributed from 0 to 1. These numbers are used to compute the polar and azimuth angles of the axis, in spherical coordinates, as $\theta = \pi r, \varphi = \text{acos}(2s - 1)$. The head was rotated around the axis Ψ_R of an angle extracted from a uniform distribution with limits equal to $\pm 10^\circ$. After the rotation, the translation along the Cartesian axes obtained by extracting each component of the displacement vector (Δx , Δy and Δz) from a uniform distribution with limits equal to ± 10 mm was applied.

In this case, being the number of input variable N equal to 6, the total number M of electromagnetic and thermal simulations, required for each XCAT model to determine the coefficients α_i of the polynomial expansion in aPC, was equal to 84.

2.7. Combined variabilities

An attempt to estimate the global uncertainty of the dosimetric quantities due to the considered variability of input data (head anatomy, tissue properties and head positioning) can be pursued following the approach here proposed.

For a given output $Y^{(r)}$ (maxSAR10g, HeadSAR, or max ΔT) associated to the anatomical model r ($r = 1, \dots, 10$), a reference value is defined, $Y_{\text{ref}}^{(r)}$, obtained with the reference input quantities (water content and head position). The corresponding PCE with respect to the water content of the four selected tissues (W_i) is known:

$$Y_{\text{PCE},W}^{(r)} = f_{\text{PCE},w}^{(r)}(W_1, W_2, W_3, W_4). \quad (6)$$

Similarly, for the PCE with respect to head positioning

$$Y_{\text{PCE},p}^{(r)} = f_{\text{PCE},p}^{(r)}(\Psi_R, \Delta x, \Delta y, \Delta z). \quad (7)$$

Expansions (6) and (7) can be normalized with respect to the reference output $Y_{\text{ref}}^{(r)}$ to obtain:

$$y_{\text{PCE},W}^{(r)} = \frac{Y_{\text{PCE},W}^{(r)}}{Y_{\text{ref}}^{(r)}}, \quad y_{\text{PCE},p}^{(r)} = \frac{Y_{\text{PCE},p}^{(r)}}{Y_{\text{ref}}^{(r)}}. \quad (8)$$

These two random variables are multiplicative correction factors whose standard deviations $u(y_{\text{PCE},W}^{(r)})$ and $u(y_{\text{PCE},p}^{(r)})$ are known.

The combined multiplicative correction factor arising when both the tissue water content and the positioning are considered simultaneously is approximated as the product of $y_{\text{PCE},W}^{(r)}$ and $y_{\text{PCE},p}^{(r)}$ by assuming the independence of the two contributions. Thus, the random output for a given anatomical model r in the most general situation is expressed as:

$$Y^{(r)} = Y_{\text{ref}}^{(r)} \cdot y_{\text{PCE},W}^{(r)} \cdot y_{\text{PCE},p}^{(r)}. \quad (9)$$

The reference value $Y_{\text{ref}}^{(r)}$ depends on the anatomy and can be considered as a categorical variable. We consider the set of values obtained with the 10 anatomical models as a continuous variable having a Gaussian distribution with mean μ_{ref} and standard deviation u_{ref} , whose numerical values are obtained in section 3.1:

$$Y_{\text{ref}} \sim \mathcal{N}(\mu_{\text{ref}}, u_{\text{ref}}). \quad (10)$$

This choice is the one with maximum entropy if mean and standard deviation are the only information available about the population (BIPM-JCGM 101:2008 2008).

Looking at the worst-case scenario (maximum variability due to tissue property variation and due to head positioning), let us now denote by $y_{\text{PCE},W}$ and $y_{\text{PCE},p}$ the random variables $y_{\text{PCE},W}^{(r)}$ and $y_{\text{PCE},p}^{(r)}$ with the largest standard deviations, so that

$$u(y_{\text{PCE},W}) = \max_r u(y_{\text{PCE},W}^{(r)})$$

and

$$u(y_{\text{PCE},p}) = \max_r u(y_{\text{PCE},p}^{(r)}).$$

Finally, the random variable Y that models the output quantity accounting for the variability introduced by the anatomical models, the tissue water content, and the head positioning is defined as

$$Y = Y_{\text{ref}} \cdot y_{\text{PCE},W} \cdot y_{\text{PCE},p}. \quad (11)$$

The statistical distribution of Y is so determined using the MC method.

3. Results

3.1. Results for reference values

One set of simulations was performed using the reference input data (tissue properties in table 3 and central head positioning). Figure 2 shows the spatial distributions of SAR10g and ΔT after 900 s in the transverse slice crossing the isocenter for the 10 head models. The corresponding values of maxSAR10g, HeadSAR and max ΔT are reported in figure 3 for all considered models.

By comparing these results with the characteristics of the XCAT models (table 1), an almost monotonic behaviour is observed for the HeadSAR versus the head mass, whereas not clear correlation is found for maxSAR10g and max ΔT . The maximum values of these two outputs are found for model #80, which gives the ‘worst case’ among the selected anatomical models.

The intersubject geometric variability leads to a maxSAR10g ranging from 0.485 W kg⁻¹ (#86) to 0.747 W kg⁻¹ (#80), to an HeadSAR from 0.159 W kg⁻¹ (#71 and #86) to 0.197 W kg⁻¹ (#184), and to a max ΔT from 0.122 K (#71) to 0.142 K (#80). The mean values (standard deviations) of the 10 reference outputs are 0.630 W kg⁻¹ (0.101 W kg⁻¹) for maxSAR10g, 0.174 W kg⁻¹ (0.012 W kg⁻¹) for HeadSAR and 0.130 K (0.007 K) for max ΔT .

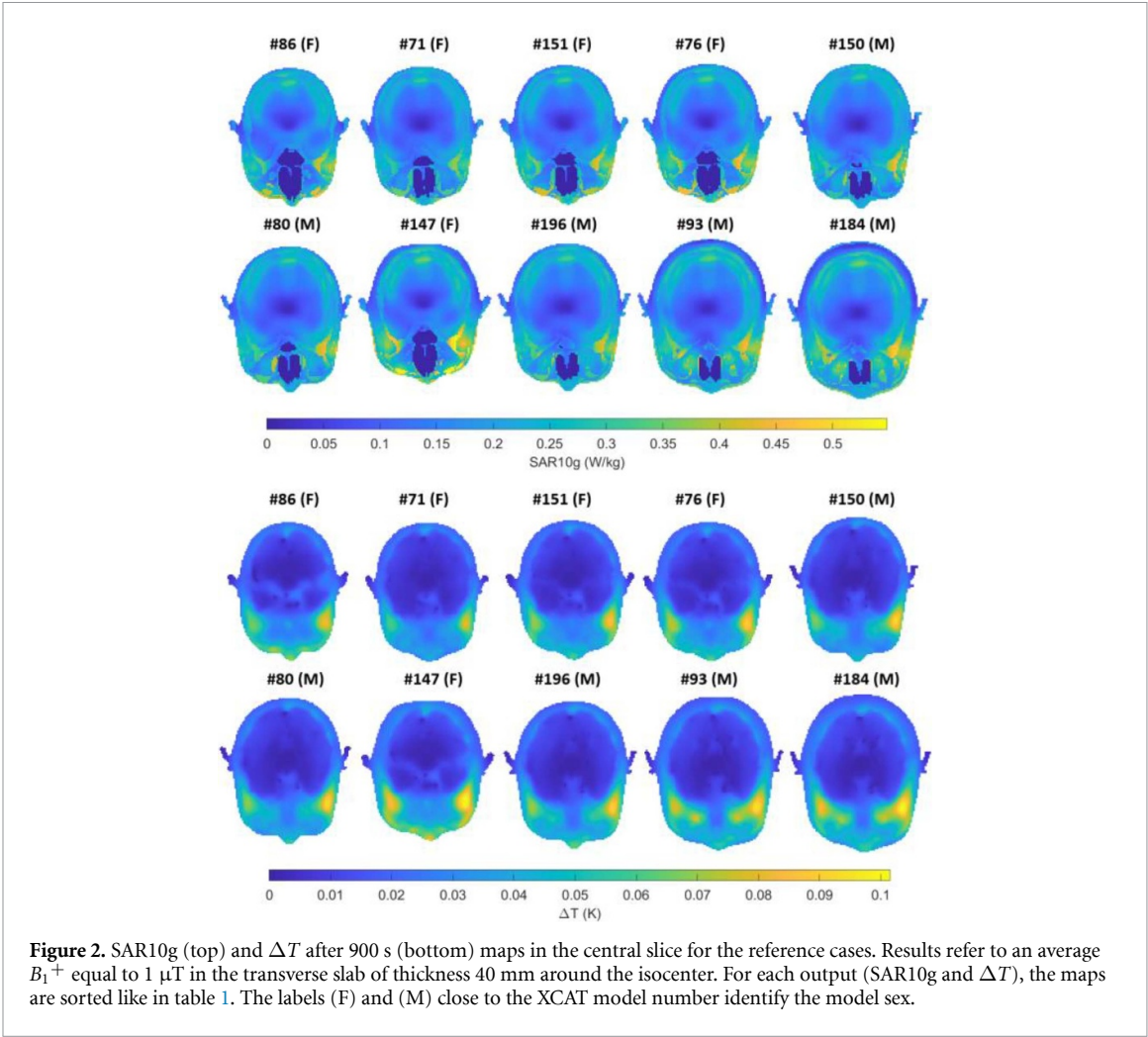


Figure 2. SAR10g (top) and ΔT after 900 s (bottom) maps in the central slice for the reference cases. Results refer to an average B_1^+ equal to 1 μ T in the transverse slab of thickness 40 mm around the isocenter. For each output (SAR10g and ΔT), the maps are sorted like in table 1. The labels (F) and (M) close to the XCAT model number identify the model sex.

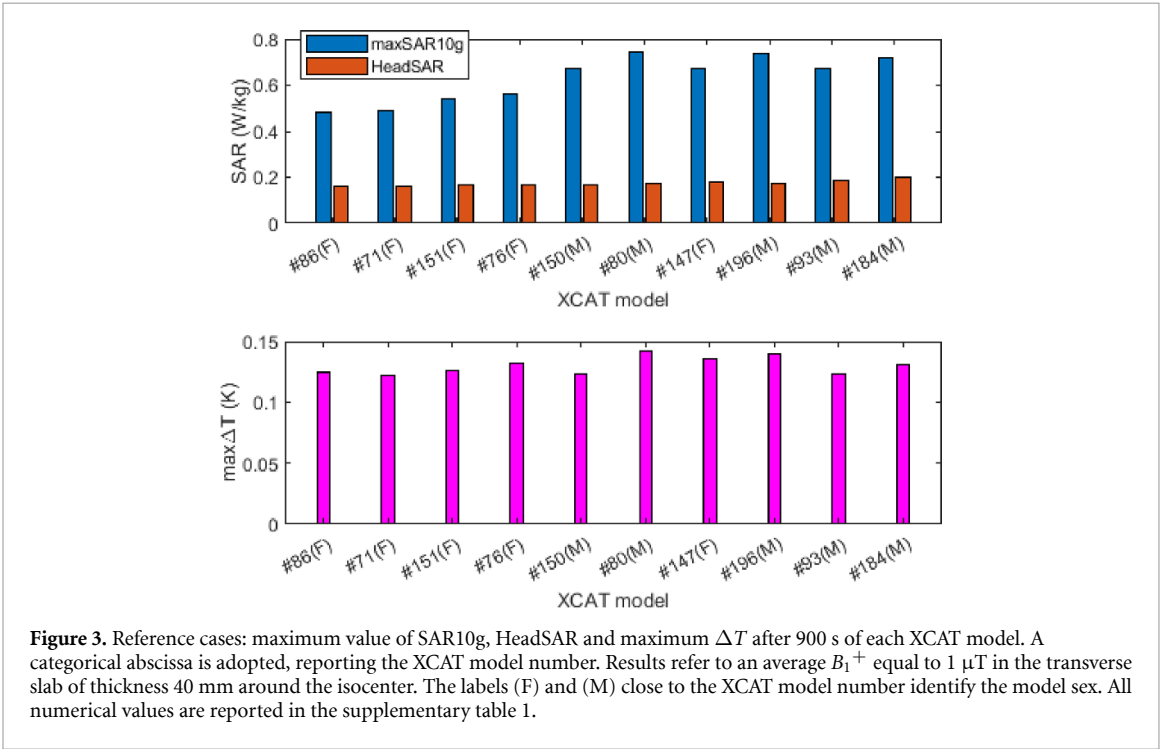


Figure 3. Reference cases: maximum value of SAR10g, HeadSAR and maximum ΔT after 900 s of each XCAT model. A categorical abscissa is adopted, reporting the XCAT model number. Results refer to an average B_1^+ equal to 1 μ T in the transverse slab of thickness 40 mm around the isocenter. The labels (F) and (M) close to the XCAT model number identify the model sex. All numerical values are reported in the supplementary table 1.

Table 4. Mean values and standard deviations of the outputs (maxSAR10g, HeadSAR and max ΔT) for model #80 considering three values for the aPC polynomial orders d .

d	No. of simulation for training (M)	maxSAR10g (W kg ⁻¹)		HeadSAR (W kg ⁻¹)		max ΔT (K)	
		Mean	StdDev	Mean	StdDev	Mean	StdDev
2	15	0.758	0.008	0.177	0.003	0.143	0.001
3	35	0.751	0.010	0.177	0.003	0.143	0.001
4	70	0.751	0.011	0.176	0.003	0.143	0.001

Table 5. Minimum and maximum values of the output quantities (maxSAR10g, HeadSAR and max ΔT) for model #80 obtained with aPC or considering two extreme cases for the tissue physical properties of the four head model districts: water content percentage equal to -4% (\underline{W}) or $+4\%$ (\bar{W}).

Case	maxSAR10g (W kg ⁻¹)		HeadSAR (W kg ⁻¹)		max ΔT (K)	
	Min	Max	Min	Max	Min	Max
aPC	0.706	0.806	0.167	0.189	0.137	0.150
\underline{W}, \bar{W}	0.742	0.763	0.167	0.188	0.141	0.145

3.2. Results for variability of tissue properties

This set of simulations was performed by considering the independent variability of water content in the four selected tissues (WM, GM, CSF, CB) with W_{ref} as reported in table 2 and W_{dev} equal to 4 % for WM, GM and CB and 1 % for CSF. For CSF the variability was limited to 1 % to avoid an unphysical upper limit for W greater than 100 %.

The corresponding lower and upper limits for the property values (whose distribution is, in general, not uniform) are:

- Electrical conductivity: (0.322 \div 0.379) S m⁻¹ for WM, (0.473 \div 0.768) S m⁻¹ for GM, (1.963 \div 2.378) S m⁻¹ for CSF, and (0.624 \div 1.159) S m⁻¹ for CB.
- Relative permittivity: (44.13 \div 59.46) for WM, (68.33 \div 77.31) for GM, (83.49 \div 83.96) for CSF, and (74.40 \div 81.07) for CB.
- Specific heat capacity: (3365 \div 3541) J kg⁻¹K⁻¹ for WM, (3669 \div 3845) J kg⁻¹K⁻¹ for GM, (4073 \div 4117) J kg⁻¹K⁻¹ for CSF, and (3779 \div 3955) J kg⁻¹K⁻¹ for CB.
- Mass density: (1084 \div 1068) kg m⁻³ for WM, (1056 \div 1040) kg m⁻³ for GM, (1019 \div 1015) kg m⁻³ for CSF, and (1046 \div 1030) kg m⁻³ for CB.
- Thermal conductivity: (0.468 \div 0.496) W m⁻¹K⁻¹ for WM, (0.517 \div 0.546) W m⁻¹K⁻¹ for GM, (0.583 \div 0.590) W m⁻¹K⁻¹ for CSF, and (0.535 \div 0.564) W m⁻¹K⁻¹ for CB.

The effect of the aPC polynomial order (d) on the stability of the results was first assessed considering the anatomical model #80. The mean value and standard deviation of maxSAR10g, HeadSAR and max ΔT , obtained with d ranging from 2 to 4, are reported in table 4. Based on these results, a polynomial order $d = 3$ was chosen for all successive simulations as a trade-off between result stability (also for the local quantity maxSAR10g) and required computational time.

The aPC coefficient values ($d = 3$), for all XCAT models are reported in the supplementary material. Figure 4 shows the box plots of the statistical distributions of the output quantities (maxSAR10g, HeadSAR and max ΔT) for the 10 considered anatomical models. The plots have been sorted by increasing mass to evidence if a correlation between the considered output quantity and mass exists.

The absolute variability due to tissue properties is almost identical for all the anatomical models when considering the HeadSAR, with a relative percentage value ranging from 1.5 % to 1.9 %. The absolute variability is more different among models for local outputs, leading to relative percentage values ranging from 0.4 % to 1.5 % for maxSAR10g and from 0.7 % to 3.3 % for max ΔT .

In table 5, the range of variation of the output parameters predicted by the aPC algorithm are compared with those obtained considering two extreme cases for the tissue physical properties of the four head model districts: water content percentage variation equal to -4% (\underline{W}) or $+4\%$ (\bar{W}). The results refer to the anatomical model #80. The comparison highlights that the range of variation of the outputs is always higher for aPC simulations, particularly for the local quantities, maxSAR10g and max ΔT . This result shows that the output variabilities predicted by using extreme values of water content percentage underestimate the actual variability.

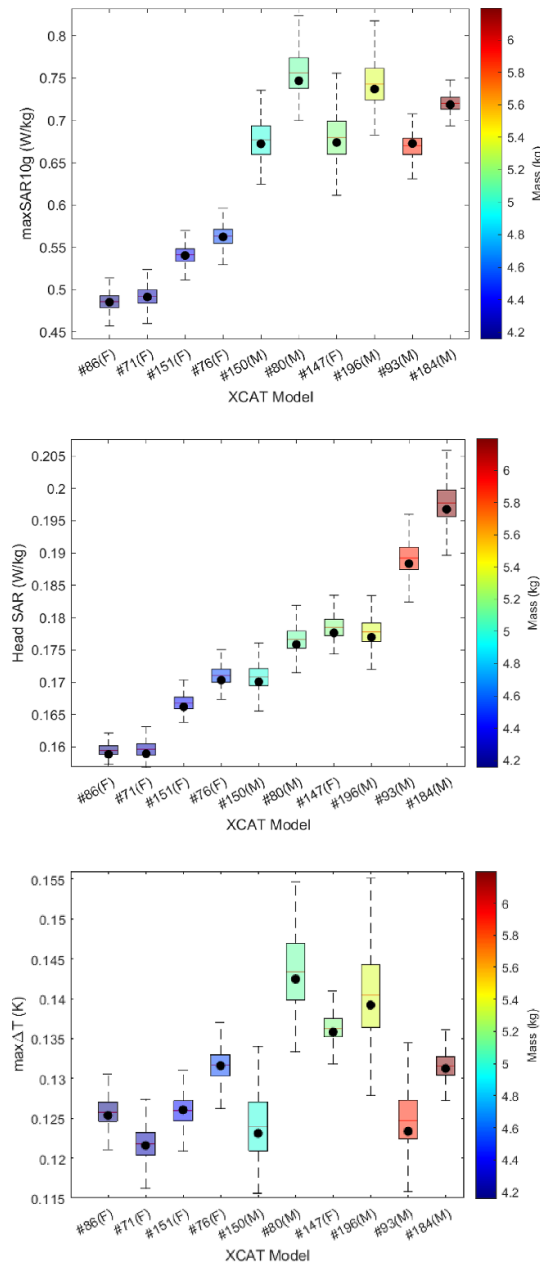


Figure 4. Box plots of the statistical distributions of the output quantities (from top to bottom, maxSAR10g, HeadSAR and max ΔT) due to the variability of the physical properties of the four brain tissues (WM, GM, CSF, CB). The box plots are sorted by increasing head mass and the colour is related to the mass scale on the right. A categorical abscissa is adopted, reporting the XCAT model number. The dots correspond to the values obtained in the reference case (figure 3). The labels (F) and (M) close to the XCAT model number identify the model sex. The mean values and standard deviations of the distributions are reported in the supplementary table 2.

Figure 5 compares the statistical distributions of the output quantities for the #80 XCAT model for $W_{\text{dev}} = 4\%$ and $W_{\text{dev}} = 8\%$. As expected, increasing the percentage variation of water content (W_{dev}) for WM, GM and CB led to an increase of the standard deviation of the output quantities.

The mean value of maxSAR10g, HeadSAR and max ΔT remained almost unchanged (0.751 W kg^{-1} , 0.177 W kg^{-1} and 0.143 K , respectively), while the standard deviations increased from 0.010 W kg^{-1} to 0.019 W kg^{-1} (for maxSAR10g), from 0.003 W kg^{-1} to 0.007 W kg^{-1} (for HeadSAR) and from 0.001 K to 0.003 K (for max ΔT).

Finally, the effect of a variability in the tissue perfusion rates on the mean values and standard deviations of max ΔT was quantified for the XCAT model #80 with a $W_{\text{dev}} = 4\%$. In particular, the tissue perfusion rate of all tissues in the anatomical model was reduced to 75 % and 50 % of the reference value of the IT²IS database. Results are summarized in table 6. It is worth observing that by halving the perfusion rate coefficient, the mean value of max ΔT is increased by +15 %, while the standard deviation is unchanged.

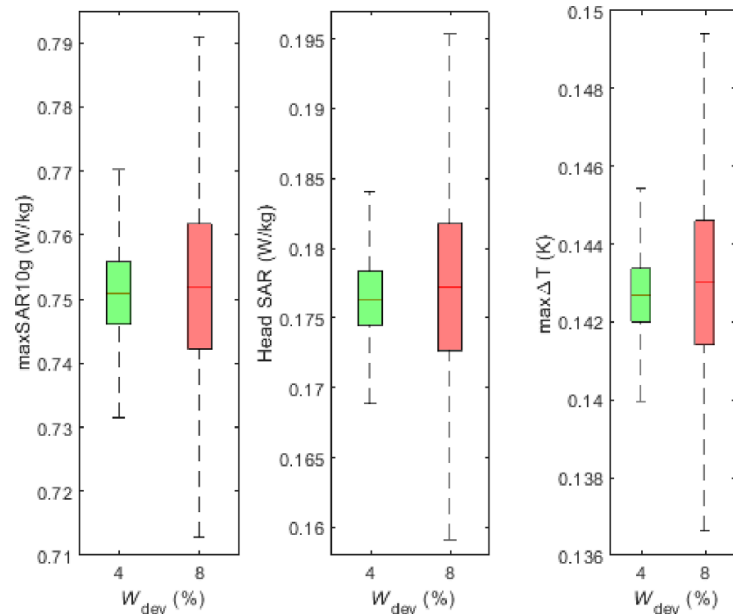


Figure 5. Comparison between the box plots of the output quantities (maxSAR10g, headSAR and max ΔT) varying W_{dev} from 4 % to 8 % for WM, GM and CB. The value was kept equal to 1% for CSF. Results refer to the XCAT model #80.

Table 6. Mean values and standard deviations of max ΔT (K) for model #80 for different reductions of the tissue perfusion rates.

Perfusion rate factor	Mean	StdDev
1 (reference values from IT'IS database)	0.143	0.001
0.75	0.152 (+6 %)	0.001
0.5	0.164 (+15 %)	0.001

3.3. Results for uncertainty in head positioning

For each XCAT model, the aPC coefficients were computed based on the 84 electromagnetic and thermal simulations (coefficient values are reported in the supplementary material). Figure 6 shows the box plots of the output quantities (maxSAR10g, HeadSAR and max ΔT) for the ten anatomical models. Similarly to figure 4, the plots are sorted by increasing mass.

The variability of the output quantities due to head positioning is similar among anatomical models for maxSAR10g and HeadSAR, whereas it is more widespread for max ΔT . This latter seems to be uncorrelated with respect to the head mass and shape. The relative percentage values range from 1.4 % to 3.7 % for maxSAR10g, from 0.6 % to 1.5 % for HeadSAR and from 1.5 % to 3.6 % for max ΔT .

3.4. Results for combined variabilities

Combined variability of the considered dosimetric quantities was determined following the approach described in section 2.7. The statistical distributions of the combined maxSAR10g, HeadSAR and max ΔT , obtained by MC method, are plotted in figure 7.

The mean values (standard deviations) of the three combined distributions are 0.630 W kg^{-1} (0.103 W kg^{-1}) for maxSAR10g, 0.176 W kg^{-1} (0.013 W kg^{-1}) for HeadSAR and 0.131 K (0.009 K) for max ΔT .

4. Discussion

A comparison between the different sources of variability in the estimated dosimetric quantities can be derived based on the results obtained by the above stochastic analysis. First, the head anatomy was found to be the most significant parameter affecting the considered output quantities, confirming results of other studies (e.g Liu *et al* 2005, Murbach *et al* 2011). The maximum percentage variation with respect to the mean value due to the geometrical differences between the anatomical models was found to be $\pm 19 \%$ for maxSAR10g (from 0.485 W kg^{-1} to 0.747 W kg^{-1}), $\pm 13 \%$ for HeadSAR (from 0.159 W kg^{-1} to 0.197 W kg^{-1}) and $\pm 10 \%$ for max ΔT (from 0.122 K to 0.142 K). As expected, the variability is lower for HeadSAR and max ΔT , the former being an integral quantity and the latter being determined by the thermal

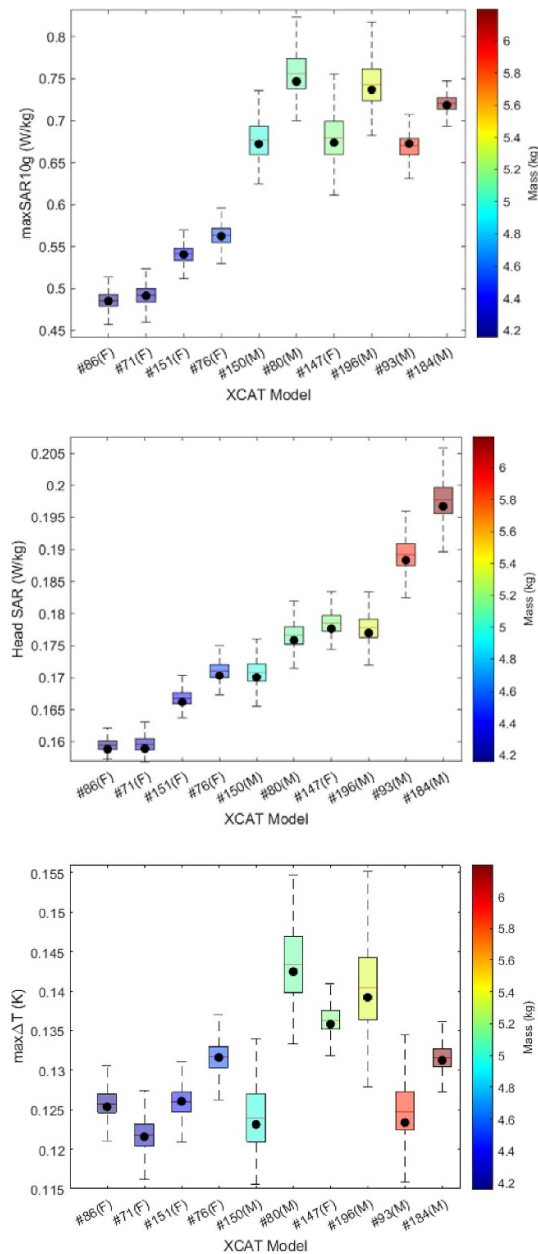


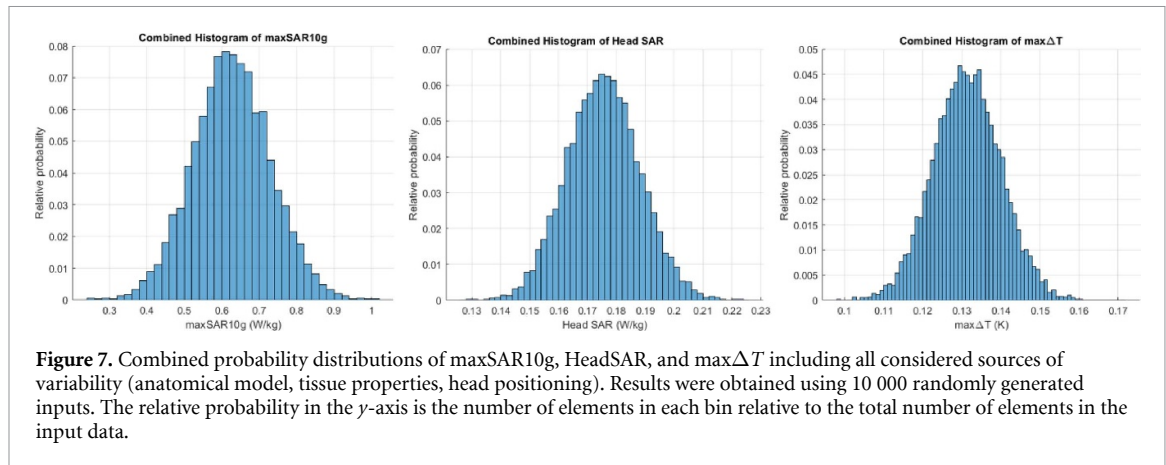
Figure 6. Box plots of the output quantities (maxSAR10g, HeadSAR and max ΔT) following the uncertainty in head positioning (roto-translation). The box plots are sorted by increasing head mass and the colour is related to the mass scale on the right. A categorical abscissa is adopted, reporting the XCAT model number. The dots correspond to the values obtained in the reference case (figure 3). The labels (F) and (M) close to the XCAT model number identify the model sex. The mean values and standard deviations of the distributions are reported in the supplementary table 3.

diffusion/perfusion process in tissues. The higher stability makes these quantities more reliable as safety metric than the maxSAR10g.

The observed variability of SAR due to the anatomy is a little bit larger than the variability observed in Liu *et al* (2019), where a deformable whole-body anatomical model, adapted to fit the patient's anatomy, is compared with the reference model in the case of thorax imaging. Indeed, in that work, the variation was 5 % on whole-body SAR and 10 % on maxSAR10g. Being assessed for head imaging, the results here presented cannot be directly extended to imaging of other anatomical regions.

By the analysis of the different models, it can also be observed a good correlation between maxSAR10g and max ΔT (minimum and maximum values are found for both quantities in models #71 e #80, respectively), while a different trend is found for HeadSAR (minimum is found in model #184 and maximum in models #71 and #86).

The intrinsic physiological variability of tissue physical properties (considering a water content variability of ± 4 %) contributes to the global variability of the output quantities with a relative standard deviation



ranging from 0.4% to 1.5 % for maxSAR10g, from 1.5 % to 1.9 % for HeadSAR and from 0.7 % to 3.3 % for max ΔT .

The local SAR variability is lower with respect to the values found in Shao *et al* (2015b), but the results cannot be directly compared because the two studies considered different MRI systems (3 T with body coil in this study, and 7 T with local RF coil in Shao *et al* (2015b) and the variability was applied to different tissues (brain tissues in this study and tissues closer to RF coil in Shao *et al* (2015b)).

Considering only the maximum values, it results that the anatomical variability has a contribution to the variability of the output quantities that is 10 times larger than the contribution due to the variability of the tissue property values for maxSAR10g (relative standard deviation of 16 % vs. 1.5 %), almost four times larger for HeadSAR (relative standard deviation of 6.9 % vs. 1.9 %) and almost two times larger for max ΔT (relative standard deviation of 5.4 % vs. 3.3 %). By doubling the variability of water content percentage, from 4 % to 8 %, the standard deviation of the output quantities almost doubles, reducing the distance from the anatomical variability contribution.

A larger contribution is the one due to the uncertainty in head positioning, which leads to a standard deviation ranging from 1.4 % to 3.7 % for maxSAR10g, from 0.6 % to 1.5 % for HeadSAR and from 1.5 % to 3.6 % for max ΔT . The weaker dependence of an integral quantity like HeadSAR to model positioning agrees with the results published in Le Garrec *et al* (2017), even if the latter refers to a 7 T head imaging.

Considering only the maximum values, this relative standard deviation is about four times lower than the one associated with the anatomical variability for maxSAR10g and HeadSAR and about two times lower for max ΔT .

In summary, the global variability of the considered dosimetric quantities due to the variability of input data (head anatomy, tissue properties and head positioning) results to be dominated by the anatomy. This is evident by comparing the standard deviation of the combined distributions and the ones deriving from the 10 reference cases. From the resulting distributions (figure 7), assuming a coverage interval of 95 %, it is reasonable to associate a global extended variability to the three considered dosimetric quantities equal to 32 % for maxSAR10g, 14 % for HeadSAR and 13 % for max ΔT . The knowledge of these variabilities can be used to attribute an uncertainty to the results obtained using a generic anatomical head model (e.g. the model giving the mean values with reference physical properties and placed in the reference position) when the SAR and temperature increase values are compared with limits for evaluating safety exposure.

When using the approach here presented to associate an uncertainty to the computation of SAR and temperature increase in a patient exposed to the field generated by the RF coil of a 3 T MRI scanner, some limitations must be considered.

First, the analysis was limited to head imaging and the results cannot be extrapolated to the entire body or to the imaging of other anatomical districts. Indeed, both the anatomy and the different tissue types could have a different impact on the distribution of power deposition and temperature increase. In addition, the dependence of tissue properties from water content here adopted was based on literature data mainly focused on brain tissues (Ahuja *et al* 1978, Michel *et al* 2016, Vaupel and Piazena 2022) and cannot be applied to other type of tissues without a proper validation. Also, the amount of variability in the model position was conceived for head imaging. For the extension to other body parts, the variability input data need to be reconsidered.

Regarding tissue physical properties, the analysis was limited by considering the variability of four clusters of head tissues. For all the other non-brain tissues, fixed values of physical properties were assigned. This choice is justified considering the attention posed to brain tissues in the definition of basic restrictions,

based on considerations related to functional changes and structural damage in the brain (IEC 60601-2-33:2022 2022).

Another limitation to be accounted for is that the analysis was conducted for 3 T imaging and with an RF body coil. While it is possible to repeat the analysis for 1.5 T MRI without changing the exposure setup, the extension at higher fields needs to reconsider the transmit coil, since a standard birdcage body coil is not typically adopted at higher frequencies. The use of a local RF coils may indeed introduce important variations on the obtained results, considering that the field distribution within the imaging volume would result in stronger heterogeneities.

The uncertainty of the output dosimetric quantities here deduced cannot be considered as an exhaustive uncertainty budget of all influence factors. Other influencing factors (e.g. RF source variability, environments, etc) can also contribute to the overall uncertainty budget. In any case, having fixed the exposure scenario, our results represent an estimate of the dosimetric simulations.

A final important remark must be considered. For practical reasons, the analysis was limited to 10 anatomical models. The models were chosen from a large library with the purpose of covering, as much as possible, the variability, in head size and shape, of adult phenotypes, as can be seen from the data in table 1. At the same time, regarding the biological tissue properties, age-related biological changes are small for adults compared to the major changes in juveniles and children. Here we have accounted for statistical tissue properties variability rather than variability consequent to the evolution process from youth to adulthood.

Anyway, all the adopted choices are inevitably incomplete and head anatomies and age-related tissue property variability can produce results that extend beyond the extreme values of the dosimetric quantities here determined (data in figure 7 and supplementary table 1).

5. Conclusions

In this study, the PCE is applied to estimate the variability of SAR and temperature increase at 3 T head MRI. Different sources of variability are considered as input: the effect of head anatomy, the stochastic variability of tissue physical properties among adult subjects and the uncertainty in model positioning within the scanner. To avoid correlation when considering the variability of tissue physical properties, as required by the adopted aPC implementation, the latter have been written as a function of tissue water content values, which are consequently used as input random variables.

For the sake of generality, the analysis was conducted normalizing the output data to an average value of B_1^+ magnitude equal to 1 μ T in a central slab. Output values can be quadratically rescaled to different values of B_1^+ .

Head anatomy was found to be the prevailing source of variability for the considered dosimetric quantities, affecting the global variability obtained by combining all contributions.

From the knowledge of the variability of SAR and temperature increase, uncertainties were associated to the data obtained using a generic anatomical head model. For the 3 T head imaging here considered, they resulted to be around 32 %, 14 % and 13 %, respectively, for maxSAR10g, HeadSAR and ΔT , with a coverage interval of 95 %.

The adopted methodology can be extended to other exposure scenarios in MRI, allowing to associate an uncertainty value to the prediction of SAR and temperature increase in tissues. The quantification of an uncertainty value associated to the estimated dosimetric quantity can be conveniently used to verify compliance with reference limits for patient safety exposure.

Data availability statement

All data that support the findings of this study are included within the article (and any supplementary information files).

Acknowledgments

The study reported in this paper is part of the field covered by the European Metrology Network (EMN) for Mathematics and Statistics. Information can be found at www.euramet.org/european-metrology-networks/mathmet/

Funding

The project (21NRM05 STASIS) has received funding from the European Partnership on Metrology, co-financed from the European Union's Horizon Europe Research and Innovation Programme and by the Participating States.

Appendix

2-D analytical model

The aPC model was preliminary tested versus a direct MC approach using a simple reference 2D problem. The availability of an analytical solution allows to limit the computational burden of the MC solution, using a sufficiently high number of random extractions.

A phantom constituted of two non-concentric cylinders aligned with the z -axis is adopted. The cylinders have an infinite length along their axes. The internal cylinder (material 2), centred in the origin, has diameter equal to 40 mm; the external cylinder (material 1) has diameter equal to 100 mm and is translated by 40 mm along the x -axis. A spatially uniform, sinusoidal magnetic flux density is applied along the z -axis.

For this 2D structure an analytical solution is available under the assumption of an unperturbed magnetic field (Polk and Song 1990), providing the spatial distribution of the induced electric field and currents in the xy -plane.

This problem, even if extremely simplified with respect to the realistic case, has some similarities with it because it describes interfaces between tissues of different electrical conductivity and the consequent change in the induced current path depending on the contact between the electrical conductivities of the two materials.

In the analysis, the electrical conductivities of material 1 and 2 were assumed to be stochastic variables. For material 1 the conductivity was chosen uniformly distributed from 0.2 S m^{-1} to 0.8 S m^{-1} , whereas for material 2 it was chosen, independently, uniformly distributed from 1.5 S m^{-1} to 2 S m^{-1} .

For aPC solution, a polynomial expansion order d equal to 3 was chosen. Since two input stochastic variables are present ($N = 2$), the number M of PCE coefficients is equal to 10. For the MC solution, results were obtained from 10 000 random extractions.

The statistical distributions obtained by MC and aPC of the output total power and maximum power density in materials 1 and 2 are compared in figure A1. Data are normalized to the square of the product between flux density amplitude and frequency. The figure shows an excellent agreement between the two approaches in terms of predicted mean, standard deviation, and statistical distribution.

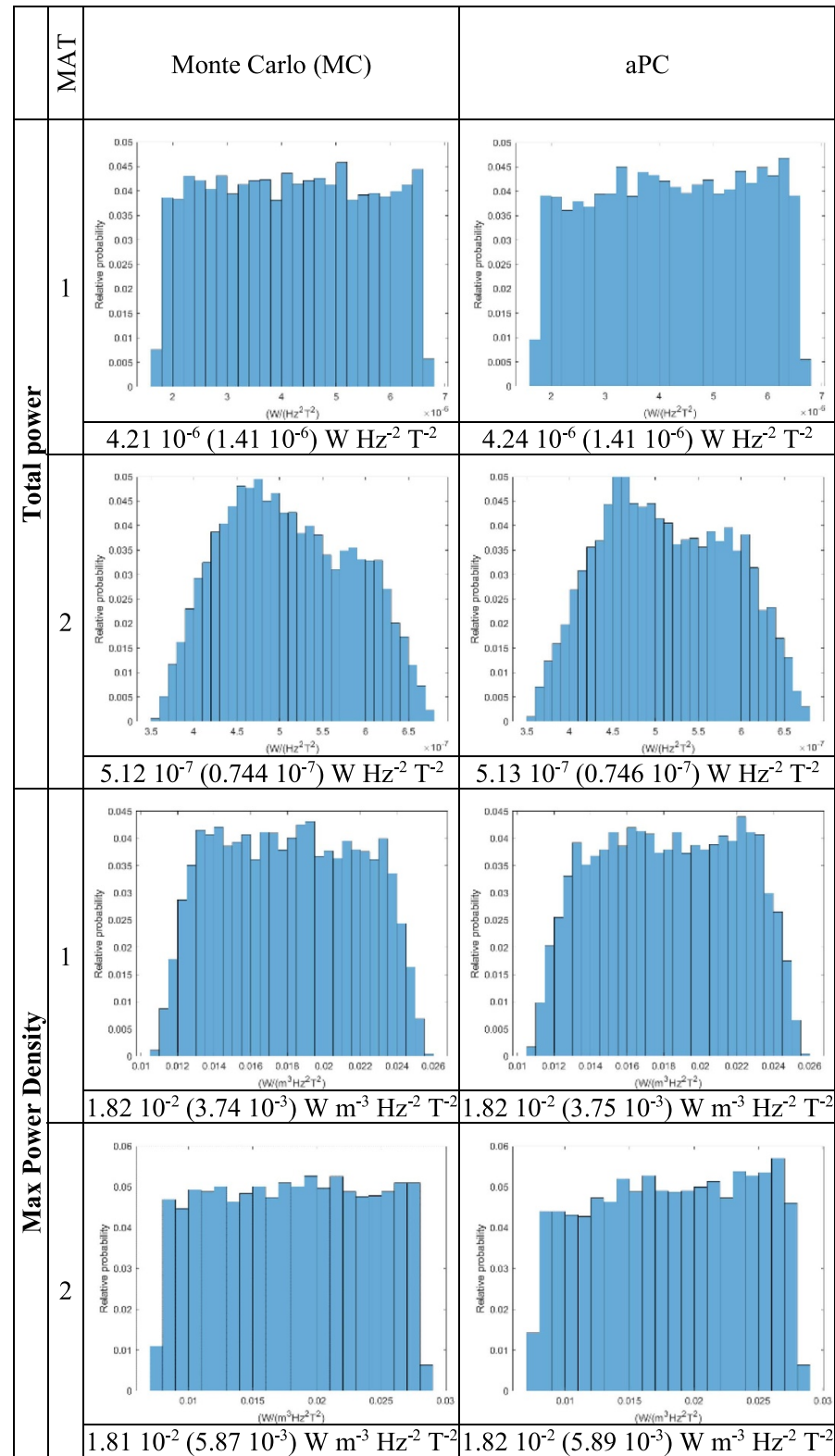


Figure A1. Reference problem involving an analytical solution: comparison between the statistical distributions of the total power and the maximum power density (normalized to the square of the product between flux density amplitude and frequency) in materials 1 and 2 computed with a direct MC (10 000 randomly generated inputs) and an aPC method. The corresponding mean value and standard deviation (in brackets) are reported under each histogram. The relative probability in the y-axis is the number of elements in each bin relative to the total number of elements in the input data.

ORCID iDs

Oriano Bottauscio <https://orcid.org/0000-0002-5437-4396>

Umberto Zanovello <https://orcid.org/0000-0001-6415-9967>

Alessandro Arduino  <https://orcid.org/0000-0002-4829-5130>

Luca Zilberti  <https://orcid.org/0000-0002-2382-4710>

References

- Ahuja A S, Prasad K N, Hendee W R and Carson P L 1978 Thermal conductivity and diffusivity of neuroblastoma tumor cells *Med. Phys.* **5** 418
- Arduino A et al 2017 Douglas–Gunn method applied to dosimetric assessment in magnetic resonance imaging *IEEE Trans. Magn.* **53** 5000204
- Augustin F, Gilg A, Paffrath M, Rentrop P and WEVER U 2008 Polynomial chaos for the approximation of uncertainties: chances and limits *Eur. J. Appl. Math.* **19** 149
- BIPM-JCGM 101:2008 2008 *Evaluation of measurement data—Supplement 1 to the “Guide to the expression of uncertainty in measurement”—Propagation of distributions using a Monte Carlo method*
- Bonato M, Dossi L, Chiaramello E, Fiocchi S, Tognola G and Parazzini M 2021 Stochastic dosimetry assessment of the human RF-EMF exposure to 3D beamforming antennas in indoor 5G networks *Appl. Sci.* **11** 1751
- Bottauscio O et al 2015 A GPU computational code for eddy-current problems in voxel-based anatomy *IEEE Trans. Magn.* **51** 5100904
- Bottauscio O, Cassarà A M, Hand J W, Giordano D, Zilberti L, Borsero M, Chiampi M and Weidemann G 2015 Assessment of computational tools for MRI RF dosimetry by comparison with measurements on a laboratory phantom *Phys. Med. Biol.* **60** 5655
- Brink W M, Yousefi S, Bhatnagar P, Remis R F, Staring M and Webb A G 2022 Personalized local SAR prediction for parallel transmit neuroimaging at 7T from a single T1-weighted dataset *Magn. Reson. Med.* **88** 464
- Carluccio G, Akgun C, Vaughan J T and Collins C 2021 Temperature-based MRI safety simulations with a limited number of tissues *Magn. Reson. Med.* **86** 543
- Chiaramello E, Le Brusquet L, Parazzini M, Fiocchi S, Bonato M and Ravazzani P 2019 3D space-dependent models for stochastic dosimetry applied to exposure to low frequency magnetic fields *Bioelectromagnetics* **40** 170
- Colella M, Paffi A, De Santis V, Apollonio F and Liberti M 2021 Effect of skin conductivity on the electric field induced by transcranial stimulation techniques in different head models *Phys. Med. Biol.* **66** 035010
- de Buck M H S, Jezzard P, Jeong H and Hess A T 2021 An investigation into the minimum number of tissue groups required for 7T in-silico parallel transmit electromagnetic safety simulations in the human head *Magn. Reson. Med.* **85** 1114
- de Greef M, Ipek O, Raaijmakers A J E, Crezee J and van den Berg C A T 2013 Specific absorption rate intersubject variability in 7T parallel transmit MRI of the head *Magn. Reson. Med.* **69** 1476
- Duke 2023 *XCAT library of anatomical models for CT imaging research* (available at: <https://otc.duke.edu/technologies/xcat-library-of-anatomical-models-for-ct-imaging-research/>)
- Fiedler T M, Ladd M E and Bitz A K 2018 SAR simulations & safety *NeuroImage* **168** 33
- Fiocchi S, Chiaramello E, Parazzini M and Ravazzani P 2018 Influence of tissue conductivity on foetal exposure to extremely low frequency magnetic fields at 50 Hz using stochastic dosimetry *PLoS One* **13** e0192131
- Gabriel S, Lau R W and Gabriel C 1996 The dielectric properties of biological tissues: II. Measurements in the frequency range 10 Hz to 20 GHz *Phys. Med. Biol.* **41** 2251
- Ghanem R G and Spanos P D 1991 *Stochastic Finite Elements: A Spectral Approach* (Springer)
- Gokyar S, Robb F J L, Kainz W, Chaudhari A and Winkler S A 2021 MRSaiFE: an AI-based approach towards the real-time prediction of specific absorption rate *IEEE Access* **9** 140824
- Gomez L J, Yucel A C, Hernandez-Garcia L, Taylor S F and Michielssen E 2015 Uncertainty quantification in transcranial magnetic stimulation via high-dimensional model representation *IEEE Trans. Biomed. Eng.* **62** 361
- Goren T, Reboux S, Farcito S, Lloyd B and Kuster N 2024 Influence of patient head definition on induced E-fields during MR examination *Magn. Reson. Med.* **91** 735
- Gräfe D, Frahm J, Merckenschlager A, Voit D and Hirsch F W 2021 Quantitative T1 mapping of the normal brain from early infancy to adulthood *Pediatr. Radiol.* **51** 450
- Hasgall P et al 2018 IT'IS database for thermal and electromagnetic parameters of biological tissues, version 4.0 *Foundation for Research on Information Technologies in Society* (available at: <https://itis.swiss/virtual-population/tissueproperties/downloads/database-v4-0/>)
- Helton J C and Davis F J 2003 Latin hypercube sampling and the propagation of uncertainty in analyses of complex systems *Reliab. Eng. Syst. Saf.* **81** 23
- Homann H, Börner P, Eggers H, Nehrke K, Dössel O and Graesslin I 2011 Toward individualized SAR models and in vivo validation *Magn. Reson. Med.* **66** 1767
- ICNIRP 2020 Guidelines for limiting exposure to electromagnetic fields (100 kHz to 300 GHz) *Health Phys.* **118** 483
- IEC 60601-2-33:2022 2022 Medical electrical equipment part 2–33: particular requirements for the basic safety and essential performance of magnetic resonance equipment for medical diagnosis
- ISO/TS 10974 2018 Assessment of the safety of magnetic resonance imaging for patients with an active implantable medical device
- Jin J, Liu F, Weber E and Crozier S 2012 Improving SAR estimations in MRI using subject-specific models *Phys. Med. Biol.* **57** 8153
- Kimaev G, Chaffart D and Ricardez-Sandoval L A 2020 Multilevel Monte Carlo applied for uncertainty quantification in stochastic multiscale systems *Process Syst. Eng.* **66** e16262
- Lagouanelle P, Choi D, Yener B and Beamer G 2024 Prediction of tuberculosis from lung tissue images of diversity outbred mice using jump knowledge based cell graph neural network *IEEE Access* **12** 17164–94
- Le Garrec M et al 2017 Probabilistic analysis of the specific absorption rate intersubject variability safety factor in parallel transmission MRI *Magn. Reson. Med.* **78** 1217
- Liu W, Collins C M and Smith M B 2005 Calculations of B1 distribution, specific energy absorption rate, and intrinsic signal-to-noise ratio for a body-size birdcage coil loaded with different human subjects at 64 and 128 MHz *Appl. Magn. Reson.* **29** 5
- Liu W, Wang H, Zhang P, Li C, Sun J, Chen Z, Xing S, Liang P and Wu T 2019 Statistical evaluation of radiofrequency exposure during magnetic resonant imaging: application of whole-body individual human model and body motion in the coil *Int. J. Environ. Res. Public Health* **16** 1069
- Lucano E, Liberti M, Lloyd T, Apollonio F, Wedan S, Kainz W and Angelone L M 2018 A numerical investigation on the effect of RF coil feed variability on global and local electromagnetic field exposure in human body models at 64 MHz *Magn. Reson. Med.* **79** 1135

- Malik S J, Beqiri A, Price A N, Teixeira J N, Hand J W and Hajnal J V 2015 Specific absorption rate in neonates undergoing magnetic resonance procedures at 1.5 T and 3 T NMR *Biomed.* **28** 344
- Maltz F H and Hitzl D L 1979 Variance reduction in Monte Carlo computations using multi-dimensional hermite polynomials *J. Comput. Phys.* **2** 345
- Martinez J A, Arduino A, Bottauscio O and Zilberti L 2023 Evaluation and correction of B_1^+ -based brain subject-specific SAR maps using electrical properties tomography *IEEE J. Electromagn. RF Microw. Med. Biol.* **7** 168
- McCann H, Pisano G and Beltrachini L 2019 Variation in reported human head tissue electrical conductivity values *Brain Topogr.* **32** 825
- Meliadò E F, van den Berg C A T, Luijten P R and Raaijmakers A J E 2019 Intersubject specific absorption rate variability analysis through construction of 23 realistic body models for prostate imaging at 7T *Magn. Reson. Med.* **81** 2106
- Michel E, Hernandez D and Lee S Y 2016 Electrical conductivity and permittivity maps of brain tissues derived from water content based on T1-weighted acquisition *Magn. Reson. Med.* **77** 1094
- Murbach M, Cabot E, Neufeld E, Gosselin M-C, Christ A, Pruessmann K P and Kuster N 2011 Local SAR enhancements in anatomically correct children and adult models as a function of position within 1.5 T MR body coil *Prog. Biophys. Mol. Biol.* **107** 428
- Murbach M, Neufeld E, Cabot E, Zastrow E, Córcoles J, Kainz W and Kuster N 2016 Virtual population-based assessment of the impact of 3 Tesla radiofrequency shimming and thermoregulation on safety and B1+ uniformity *Magn. Reson. Med.* **76** 986
- Murbach M, Neufeld E, Kainz W, Pruessmann K P and Kuster N 2014 Whole-body and local RF absorption in human models as a function of anatomy and position within 1.5T MR body coil *Magn. Reson. Med.* **71** 839
- Neufeld E, Gosselin M-C, Murbach M, Christ A, Cabot E and Kuster N 2011 Analysis of the local worst-case SAR exposure caused by an MRI multi-transmit body coil in anatomical models of the human body *Phys. Med. Biol.* **56** 15
- Nguyen B T, Pilitsis J and Golestanirad L 2020 The effect of simulation strategies on prediction of power deposition in the tissue around electronic implants during magnetic resonance imaging *Phys. Med. Biol.* **65** 185007
- Oladyshkin S 2024 aPC matlab toolbox: data-driven arbitrary polynomial Chaos, version 1.0.9 (available at: <https://ch.mathworks.com/matlabcentral/fileexchange/72014-apc-matlab-toolbox-data-driven-arbitrary-polynomial-chaos>)
- Oladyshkin S, de Barros F P J and Nowak W 2012 Global sensitivity analysis: A flexible and efficient framework with an example from stochastic hydrogeology *Adv. Water Resour.* **37** 1508
- Oladyshkin S and Nowak W 2012 Reliability Engineering and System Safety *Reliab. Eng. Syst. Saf.* **106** 179
- Pennes H H 1948 Analysis of Tissue and Arterial Blood Temperatures in the Resting Human Forearm *J. Appl. Physiol.* **1** 93
- Polk C and Song J H 1990 Electric fields induced by low frequency magnetic fields in inhomogeneous biological structures that are surrounded by an electric insulator *Bioelectromagnetics* **11** 235
- Shao Y, Shang S and Wang S 2015a On the safety margin of using simplified human head models for local SAR simulations of B1-shimming at 7 Tesla *Magn. Reson. Imaging* **33** 779
- Shao Y, Zeng P and Wang S 2015b Statistical simulation of SAR variability with geometric and tissue property changes by using the unscented transform *Magn. Reson. Med.* **73** 2357
- Sudret B *et al* 2008 Global sensitivity analysis using polynomial chaos expansions *Reliab. Eng. Syst. Saf.* **93** 964
- Šušnjara A, Dodig H, Cvetković M and Poljak D 2020 Stochastic dosimetry of a three compartment head model *Eng. Anal. Bound. Elem.* **117** 332
- Vaupel P and Piazena H 2022 Strong correlation between specific heat capacity and water content in human tissues suggests preferred heat deposition in malignant tumors upon electromagnetic irradiation *Int. J. Hyperthermia* **39** 987
- Wiener N 1938 The Homogeneous Chaos *Am. J. Math.* **60** 897
- Wolf S, Diehl D, Gebhardt M, Mallow J and Speck O 2013 SAR simulations for high-field MRI: How much detail, effort, and accuracy is needed? *Magn. Reson. Med.* **69** 1157
- Xikai C, Liu Q and Wang Y 2019 Uncertainty of geomagnetically induced current in Xinjiang 750kV planned power grid based on polynomial chaos expansion *J. Phys.: Conf. Ser.* **1237** 042015
- Xiu D and Karniadakis G E 2002 The Wiener–Askey polynomial Chaos for stochastic differential equations *SIAM J. Sci. Comput.* **24** 619